BISTABLE REFLECTIVE ETALON (BRET)

Sarnoff Corporation

APPROVED FOR PUBLIC RELEASE; DISTRIBUTION UNLIMITED.

AIR FORCE RESEARCH LABORATORY
SENSORS DIRECTORATE
ROME RESEARCH SITE
ROME, NEW YORK

This report has been reviewed by the Air Force Research Laboratory, Information Directorate, Public Affairs Office (IFOIPA) and is releasable to the National Technical Information Service (NTIS). At NTIS it will be releasable to the general public, including foreign nations.

AFRL-SN-RS-TR-2003-210 has been reviewed and is approved for publication.

APPROVED: /s/
            JAMES R. HUNTER
            Project Engineer

FOR THE DIRECTOR: /s/
            RICHARD G. SHAUGHNESSY, LtCol., USAF, Chief
            Rome Operations Office
            Sensors Directorate

REPORT DOCUMENTATION PAGE

Form Approved
OMB No. 074-0188

1. AGENCY USE ONLY (Leave blank)	2. REPORT DATE SEPTEMBER 2003	3. REPORT TYPE AND DATES COVERED Final Jul 02 – Jan 03	

4. TITLE AND SUBTITLE
BISTABLE REFLECTIVE ETALON (BRET)

6. AUTHOR(S)
Zane Shellenbarger and Joseph H. Abeles

5. FUNDING NUMBERS
C - F30602-02-C-0162
PE - 62204F
PR - 2002
TA - SN
WU - 07

7. PERFORMING ORGANIZATION NAME(S) AND ADDRESS(ES)
Sarnoff Corporation
201 Washington Road
Princeton New Jersey 08543

8. PERFORMING ORGANIZATION REPORT NUMBER

N/A

9. SPONSORING / MONITORING AGENCY NAME(S) AND ADDRESS(ES)
Air Force Research Laboratory/SNDP
25 Electronic Parkway
Rome New York 13441-4514

10. SPONSORING / MONITORING AGENCY REPORT NUMBER

AFRL-SN-RS-TR-2003-210

11. SUPPLEMENTARY NOTES

AFRL Project Engineer: James R. Hunter/SNDP/(315) 330-7045/ James.Hunter@rl.af.mil

12a. DISTRIBUTION / AVAILABILITY STATEMENT
APPROVED FOR PUBLIC RELEASE; DISTRIBUTION UNLIMITED.

12b. DISTRIBUTION CODE

13. ABSTRACT *(Maximum 200 Words)*
This project designed, fabricated, and characterized normal-incidence etalon structures at 1550 nm wavelength operation for application, as bistable elements, to photonic analog-to-digital conversion. The semiconductor devices consist of planar multi-quantum well saturable absorbers situated within an etalon defined by epitaxially grown reflective distributed Bragg reflector mirrors. Two iterations were completed and characterized in a transmissive configuration of greatest interest to Air Force Research Laboratories. Nonlinear transmission was observed. Bistability could not be obtained. Detailed modeling showed that thermal mechanisms override the quantum well nonlinearity, even at sub-nsec time scales, owing to the very small size of the etalon (several microns). However, waveguide configurations, with longer optical paths (hundreds of microns or larger), are well-suited for bistability, as demonstrated both through modeling and experimental results. Results of this effort suggest that the main obstacle to bistability in the BRET structure was heating effects. It is concluded that a future approach is to use bistable ridge waveguides instead of bistable vertical cavities. Bistability has been observed in such devices fabricated for other purposes.

14. SUBJECT TERMS
Bistable Reflective Etalon, Optical Reflector, Multiple Quantum Well Mirror, Saturable Absorbers

15. NUMBER OF PAGES
25

16. PRICE CODE

17. SECURITY CLASSIFICATION OF REPORT	18. SECURITY CLASSIFICATION OF THIS PAGE	19. SECURITY CLASSIFICATION OF ABSTRACT	20. LIMITATION OF ABSTRACT
UNCLASSIFIED	UNCLASSIFIED	UNCLASSIFIED	UL

NSN 7540-01-280-5500

Standard Form 298 (Rev. 2-89)
Prescribed by ANSI Std. Z39-18
298-102

TABLE OF CONTENTS

LIST OF FIGURES

LIST OF TABLES

Abstract

During this program, Sarnoff Corporation designed, fabricated, and characterized normal-incidence etalon structures for 1550 nm wavelength operation for application, as bistable elements, to photonic analog-to-digital conversion. The semiconductor devices consist of planar multi-quantum well saturable absorbers situated within an etalon defined by epitaxially grown reflective distributed Bragg reflector mirrors. Two iterations were completed and characterized in a transmissive configuration of greatest interest to Air Force Research Laboratories. Nonlinear transmission was observed. Bistability could not be obtained. Detailed modeling showed that thermal mechanisms override the quantum well nonlinearity, even at sub-nsec time scales, owing to the very small size of the etalon (several microns). However, waveguide configurations, with longer optical paths (hundreds of microns or larger), are well-suited for bistability, as demonstrated both through modeling and experimental results.

Technical Results

Initial Modeling and Low-Temperature Growth

InGaAs/InAlAs MQW stacks have been used previously at AFRL for saturable absorbers and this material was examined as an initial design for the absorbing part of the BRET structure. To calculate the properties of this material a previously developed model for electroabsorbtive modulators was modified for this program. Band parameters for the AlGaInAsP material system were added to the existing modeling software. Optical absorption spectra were calculated for two variations of the structure as shown in Figure 1.
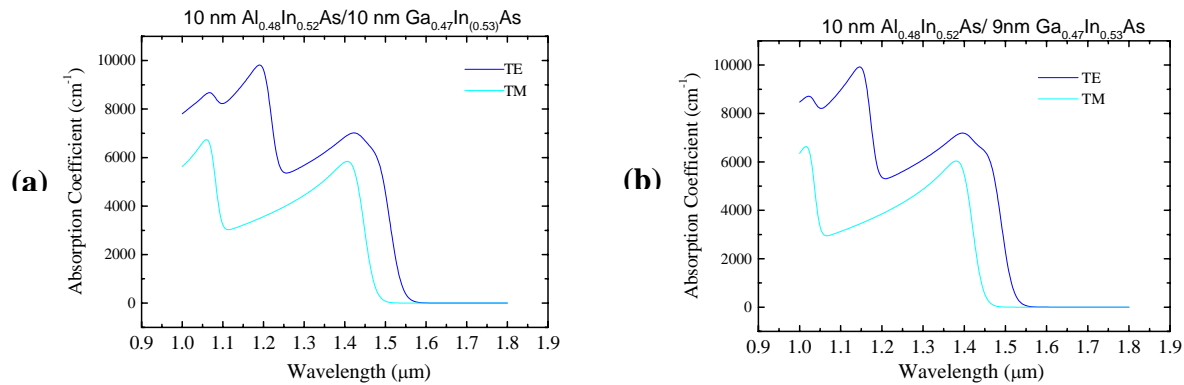
Figure 1. Calculated absorption coefficient of InGaAs/InAlAs structures with (a) 10 nm well thickness, and (b) 9 nm well thickness.

Initial calibration samples of the InGaAs/InAlAs MQW stacks were fabricated. The nonlinear transmission and the recovery time or lifetime of the carriers within the semiconductor are the most important parameters for this application. Literature suggests that low temperature growth should decrease the recovery time. Growth of InGaAs and InAlAs was calibrated at the low growth temperature of approximately 450 °C. Normal growth temperature used for these materials is 675 °C. A large increase in the source flowrates for the Al and Ga was necessary at this low temperature. Two saturable absorber samples were grown. Both have 50 pairs of the

InGaAs QW/InAlAs barrier for a total thickness of about 1 micron followed by a 100 nm InP cap layer. The main difference between the two samples is a shift in the photoluminescence. Sample AX5090 has peak PL of 1590 nm, while AX5093 has a peak PL of 1502 nm. Sample AX5090 has nominal thickness of 10 nm for both the well and barriers. Sample AX5093 has well thickness of 9 nm and barrier thickness of 10 nm. The model shows that such a large shift in wavelength should not be due to QW thickness alone. The additional red shift in sample AX5090 is due to compressive strain in the QW as confirmed by X-ray diffraction measurements. The wafers were backside polished and one ½ wafer of each sample was delivered to AFRL for testing. Measurements were conducted at Sarnoff on the remaining ½ wafers.

The absorption coefficient shown in Figure 1 was calculated with an initial estimation of 25 meV excitonic broadening. Experimentally measured data on the low temperature growth samples however, suggested a much larger broadening energy of ~60 meV. Figure 2 compares the modeled and measured absorption coefficient spectrum assuming such broadening. Although the model appears to predict the band edge properly, it clearly deviates from the measured data above and below the band edge.
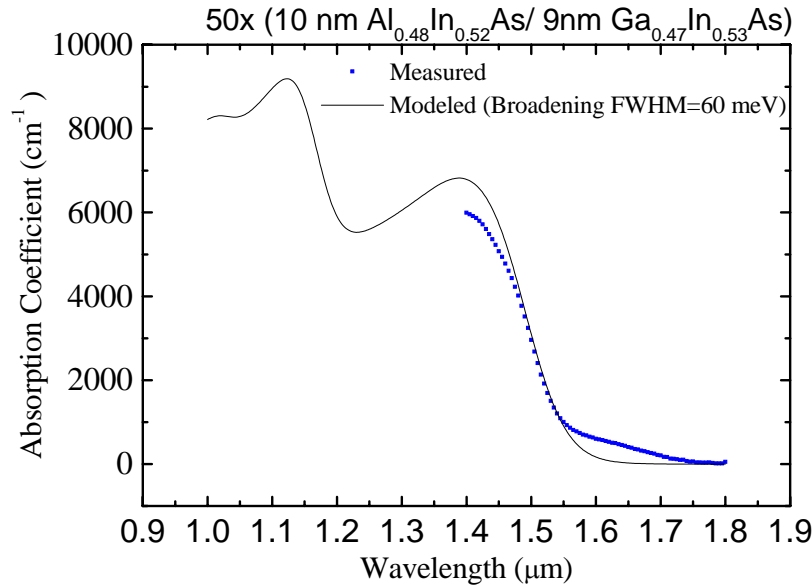
Figure 2. Modeled optical absorption coefficient spectrum versus experimentally measured data points for the sample with 9 nm quantum wells.

Fabry-Perot (FP) oscillation was identified as a possible reason for such deviations, since some of the longer scans show multiple peaks above the band edge, where no absorption features should exist. FP oscillation with such long wavelength periods can only be originated from cavities in the micrometer range, and hence we modeled the effect of slight difference of index of the multi-quantum well (MQW) region and the substrate. Unfortunately, it is not easy to model the index of the quantum wells, especially for the wavelengths shorter than the band edge. A good approximation below the band edge however, is the refractive index of a quaternary with a similar band edge.

We used the wavelength dependent index of InGaAsP with a bandgap of 0.826 eV based on a calculation by Henry et al[1]. Figure 3 shows the result of the calculated optical transmission without and with the FP effect. The model that includes the FP effect shows very good agreement to the measured data at longer wavelength and gradually deviates from it near the band edge. The best fit was obtained for a MQW region with a thickness of 1.03 μm, which is very close to the nominal 1 μm value.
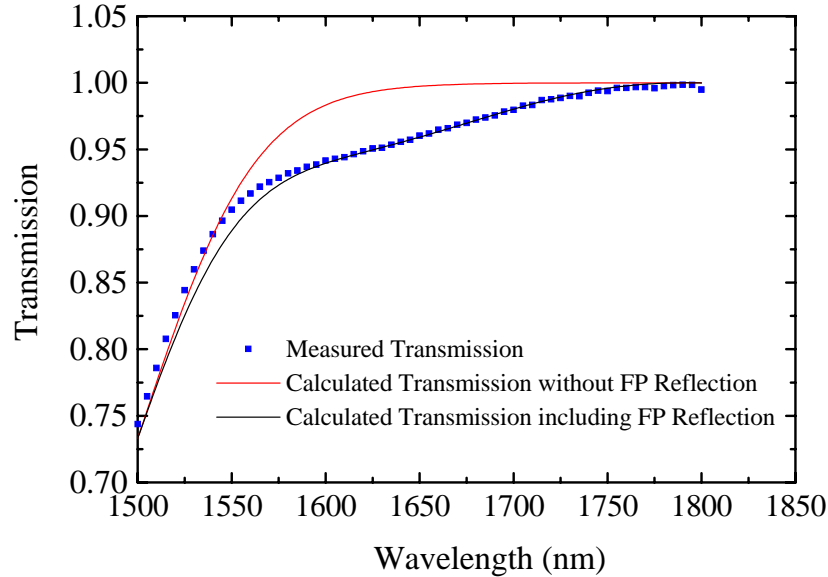

Figure 3. Measured optical transmission spectrum compared to the modeled data without (red) and with (black) the effect of FP oscillation in the MQW region.

The low temperature growth was designed to decrease the recovery time but has a trade off with lower material quality that may lead to low transmission of light. Two similar samples were grown at 675 °C, which is our normal growth temperature used for these materials. The only difference in the structure is that the 100 nm InP cap layer was replaced with another 10 nm InGaAs layer. Figure 4 compares double crystal X-ray diffraction measurements for the samples grown at low and high temperature. The X-ray peaks from the high temperature sample are higher in intensity and much sharper, indicating good layer uniformity and sharp interfaces. Figure 5 compares the photoluminescence (PL) for the samples grown at low and high temperature. The PL peak for the high temperature growth is much narrower and the intensity is increased by more than two orders of magnitude, indicating much higher material quality. The wafers were backside polished and one ½ wafer of each sample was delivered to AFRL for testing. Measurements were conducted at Sarnoff on the remaining ½ wafers.

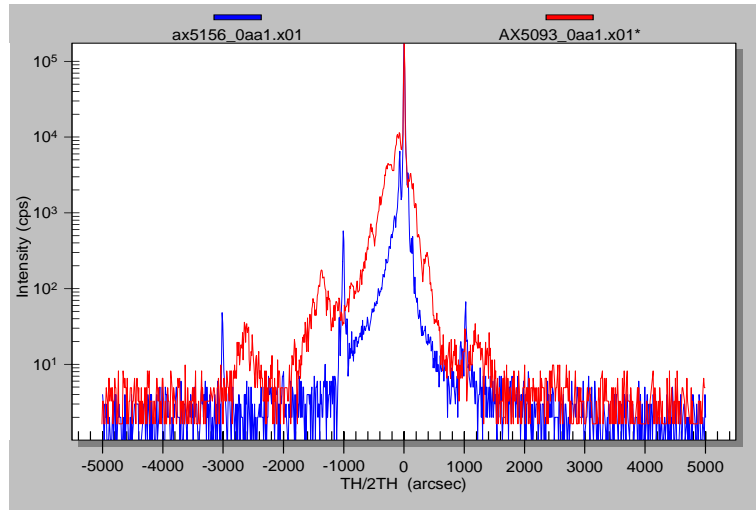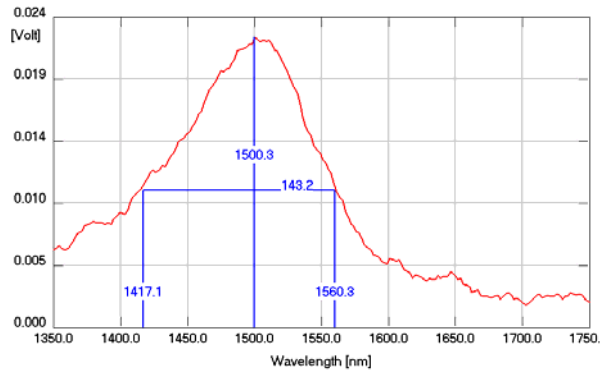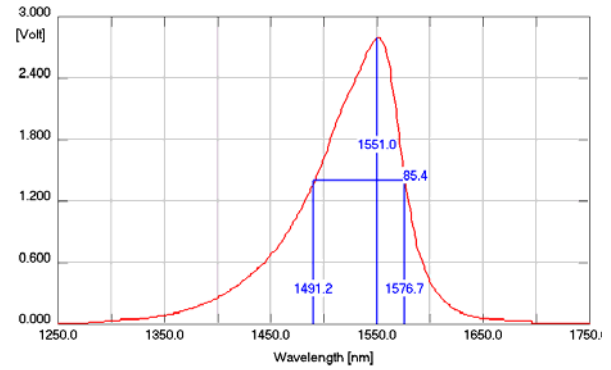[1] C.H. Henry, J. of Quant. Elect., QE-21, 12 (1985) 1887-1892

Figure 4. X-ray diffraction data of low (AX5093) and high (AX5156) temperature samples.

| (a) | (b) |

Figure 5. PL of (a) low temperature (AX5093) and (b) high temperature (AX5157) samples.

First Growth Iteration

First Iteration Design

After discussion with AFRL it was agreed that Sarnoff would go ahead with design of the whole bistable reflective etalon (BRET) structure at our normal higher growth temperature based on the existing measurement data. The model used for the saturable absorber was expanded to include the effects of the etalon. The procedure used for modeling the output versus input of the BRET device is given in TABLE 1. The bistability of different structures was modeled. A final design for the first iteration of the BRET structure was agreed upon.

TABLE 1: Modeling Procedure for BRET Device

1- Calculate $\alpha(\lambda,N)$
2- Calculate $\alpha(\lambda,I_c)$ using iterative methods (I_c is the optical intensity inside the cavity)
3- Calculate $\Delta n(\lambda,I_c)$ using Kromers-Kronig
4- Calculate cavity internal phase change $\Delta\phi=\Delta nk_0L$
5- Calculate input optical intensity $I_{IN}=C(1+F\sin(\phi)^2)I_c$ where:
    $C=\alpha L(1-R_e)^2/[(1-R_F)(1+R_Be^{-\alpha L})(1-e^{-\alpha L})]$
    $F=4R_e/(1-R_e)^2$
    $R_e=(R_FR_B)^{0.5}e^{-\alpha L}$
    L= cavity length
    R_B= back mirror reflectivity
    R_F= front mirror reflectivity
6- Calculate output optical intensity $I_{out}=I_c\alpha L(1-R_B)e^{-\alpha L}/[(1-e^{-\alpha L})(1+R_Be^{-\alpha L})]$
7- Plot output optical intensity vs. input optical intensity.

Modeling results of $\alpha(\lambda,N)$ as in Step 1 are shown in Figure 6.
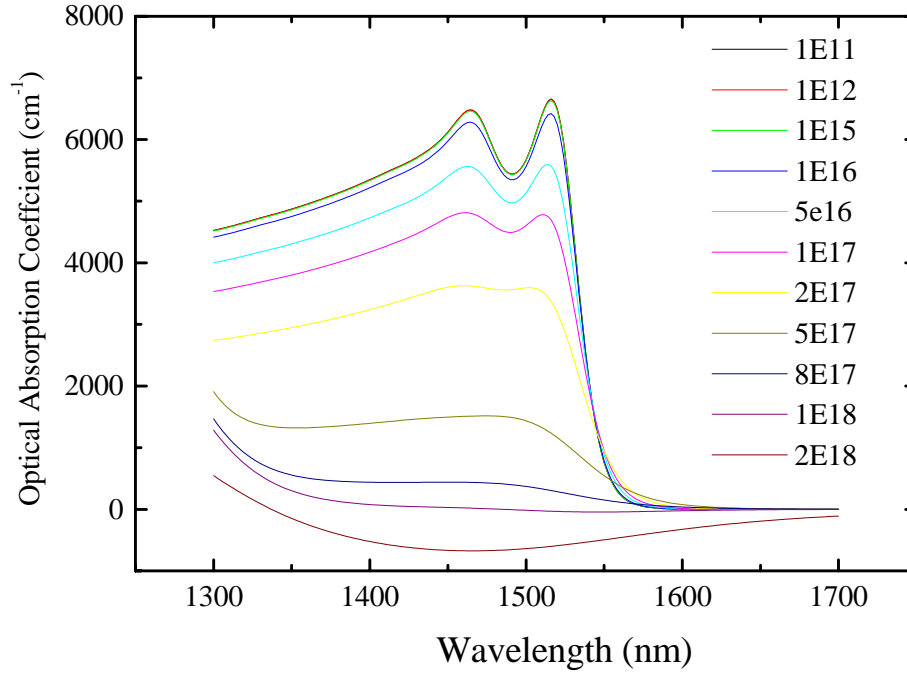

Figure 6. Modeling of absorption coefficient versus wavelength for different carrier densities.

Results of the modeling showed that with the right parameters for the front and back mirrors and the cavity length, bistability should be obtainable in a particular wavelength range. The results of one such set of parameters according the modeling are shown in Figure 7.
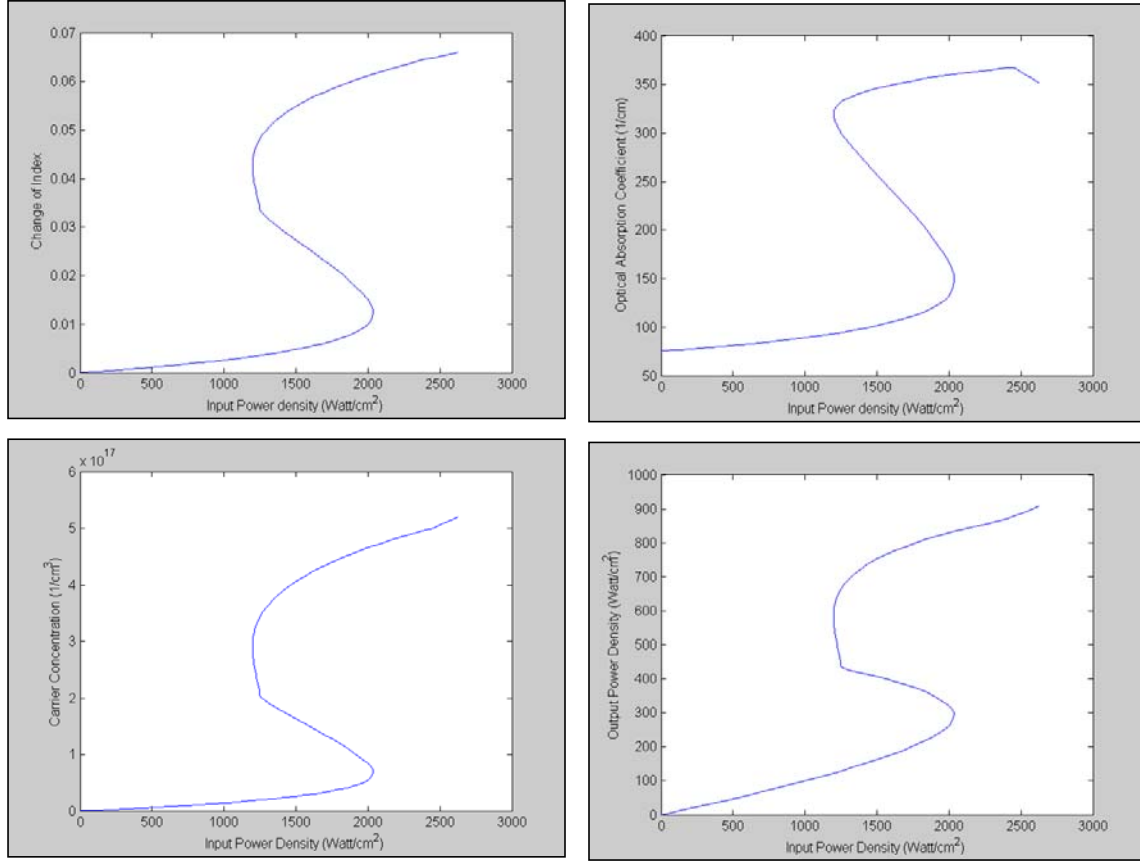
$R_B=98\%$; $R_F=95\%$; $L=0.25$ μm; $\lambda=1.575$ μm; $\tau=2$ ns

Figure 7. Results of BRET modeling showing bistability.

Following initial modeling, the sensitivity of the bistability versus the different parameters was studied. The performance of the device is very sensitive to cavity length as shown in Figure 8. A few nanometer variation in the thickness has a very large influence on the bistability. The bistability characteristics are much less sensitive to wavelength and front mirror reflectivity as shown in Figures 9 and 10.

L=0.249 μm

λ=1.570 μm

L=0.250 μm

λ=1.575 μm

L=0.251 μm

R_B=98%, R_F=95%, λ=1.575 μm, τ=2 ns

λ=1.580 μm
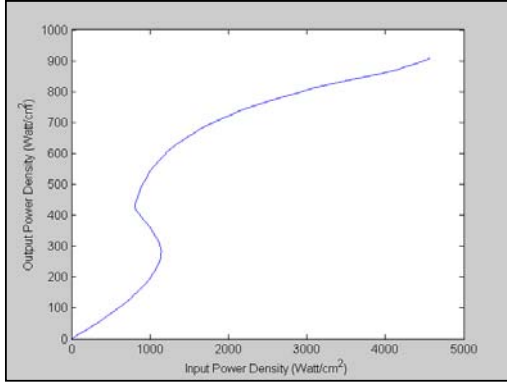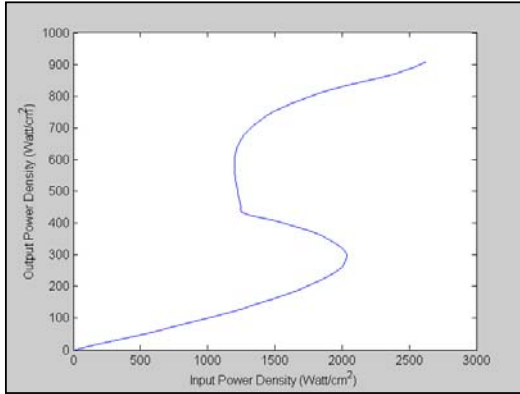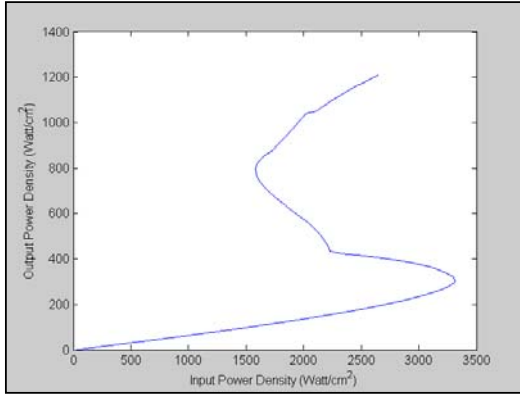
R_B=98%, R_F=95%, L=0.25 μm, τ=2 ns

Figure 8. Sensitivity of modeled bistability to cavity length.
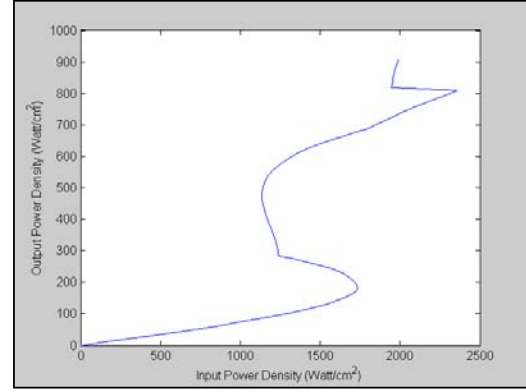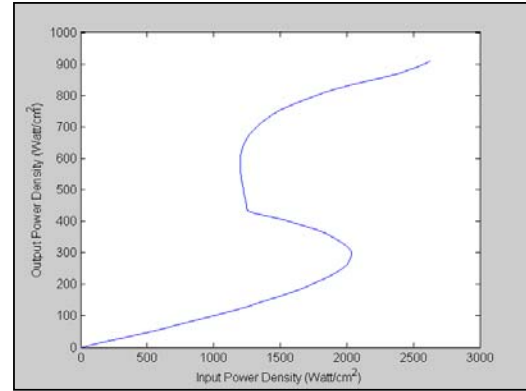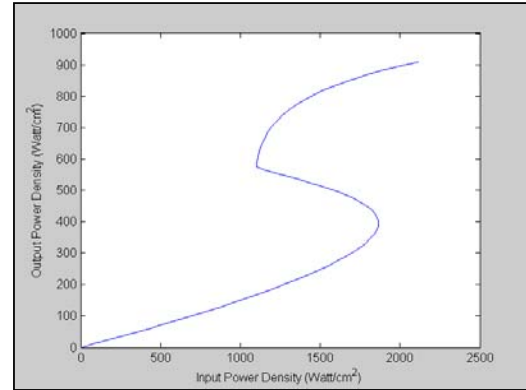
Figure 9. Sensitivity of modeled bistability to wavelength.

$R_F=96\%$

$R_F=95\%$

$R_F=94\%$

$R_F=90\%$

$R_F=80\%$

$R_B=98\%$
$L=0.25\ \mu m$
$\lambda=1.575\ \mu m$
$\tau=2\ ns$
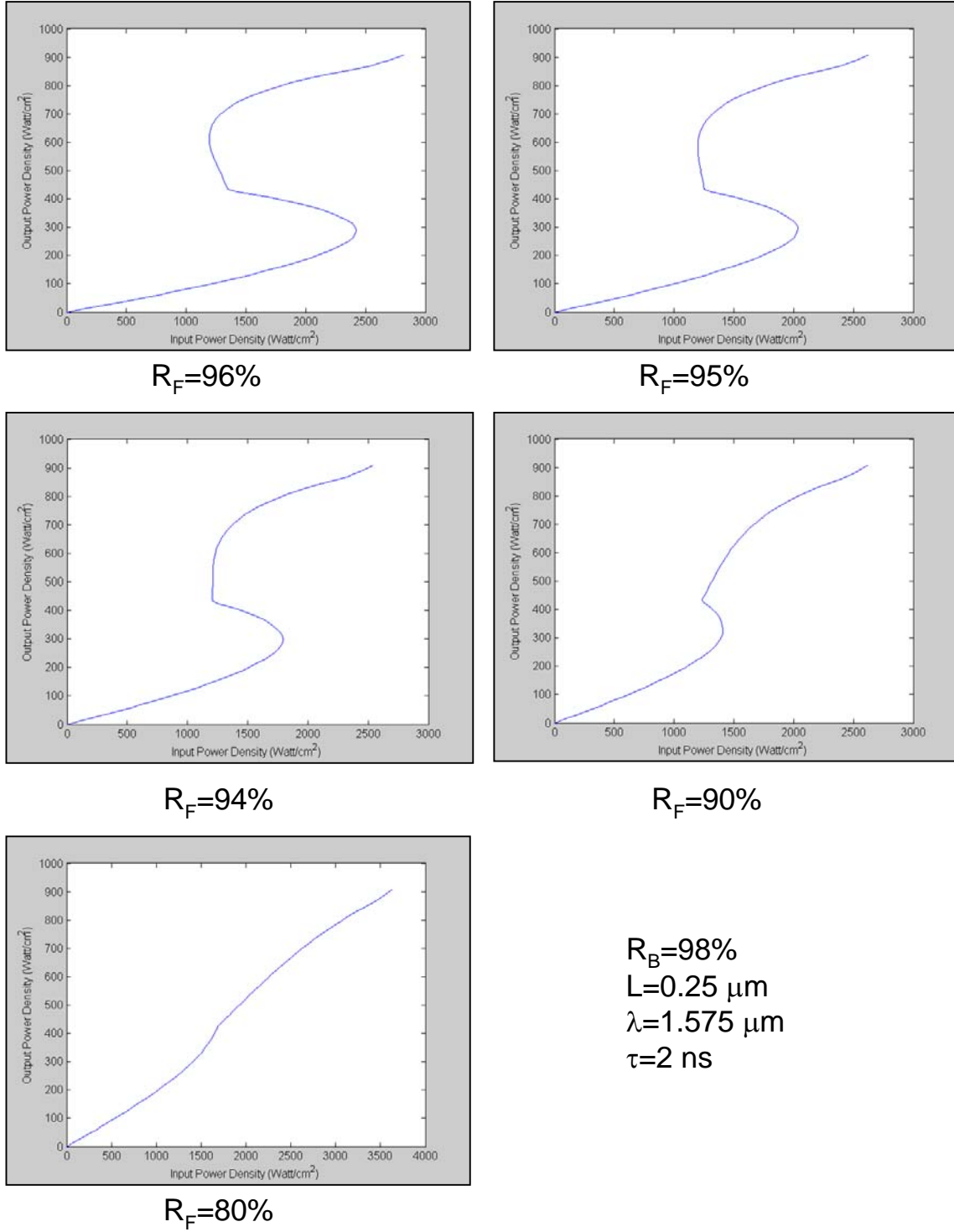
Figure 10. Sensitivity of modeled bistability to front mirror reflectivity.

After discussion with AFRL, a final design for the first iteration of the BRET structure was agreed upon. The basic design of the etalon is front mirror (epitaxially grown DBR) reflectivity of 95%, back mirror (dielectric stack) reflectivity of 98% and a cavity length of

360 nm. A schematic of the design is shown in Figure 11. The cavity is made up of the same InGaAs/AlInAs MQW saturable absorber material used in previous structures but with absorption shifted 20 nm shorter by decreasing the InGaAs QW thickness.
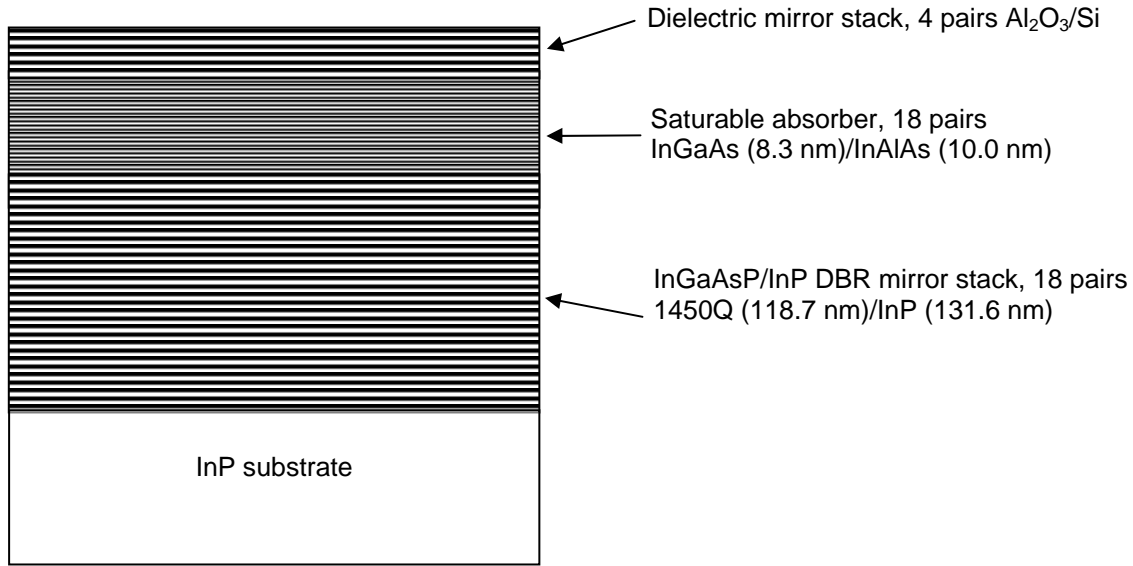
Note: 1450Q refers to InGaAsP with a photoluminescence of 1450 nm.

Figure 11. Structure of BRET device.

Fabrication of BRET Device

The DBR mirror is composed of alternating InP and InGaAsP having bandgap wavelength of 1450 nm (1450Q). The designed InP thickness is 131.6 nm and the 1450Q thickness is 118.7 nm with 18 pairs for peak reflectivity of ~95%. The mirror layer composition was calibrated and the peak reflectivity was adjusted by changing the layer thicknesses. The reflectivity result for an 18 pair mirror is shown in Figure 12. It has a peak reflectivity of 96% at 1540 nm. In the full BRET structures the thickness was increased slightly to shift the peak reflectivity to 1555 nm.
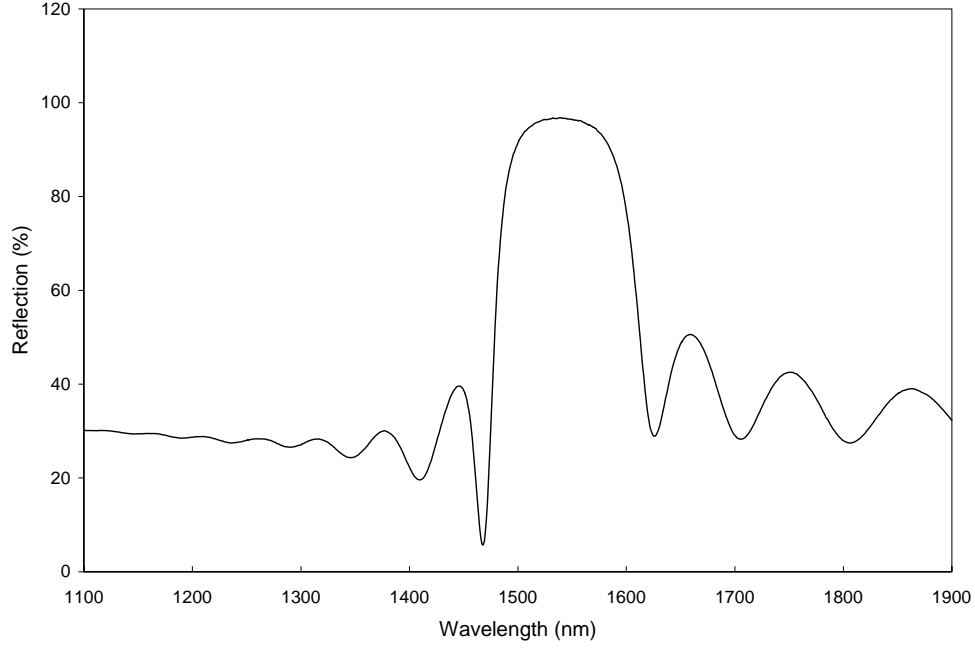
Figure 12. Reflectivity spectrum for 18 pair InP/Q1450 DBR.

To optimize for a wavelength of 1555 nm the absorption of the InGaAs/AlInAs MQWs needed to be shifted by ~20 nm from the previous material. This was done by reducing the thickness of the InGaAs QW and measuring the shift in the transmission measurement curves. Figure 13 compares transmission measurement results from a 50 pair saturable absorber growth (AX5259) having 9 nm thick InGaAs QW compared to the previous material with 10 nm QW.
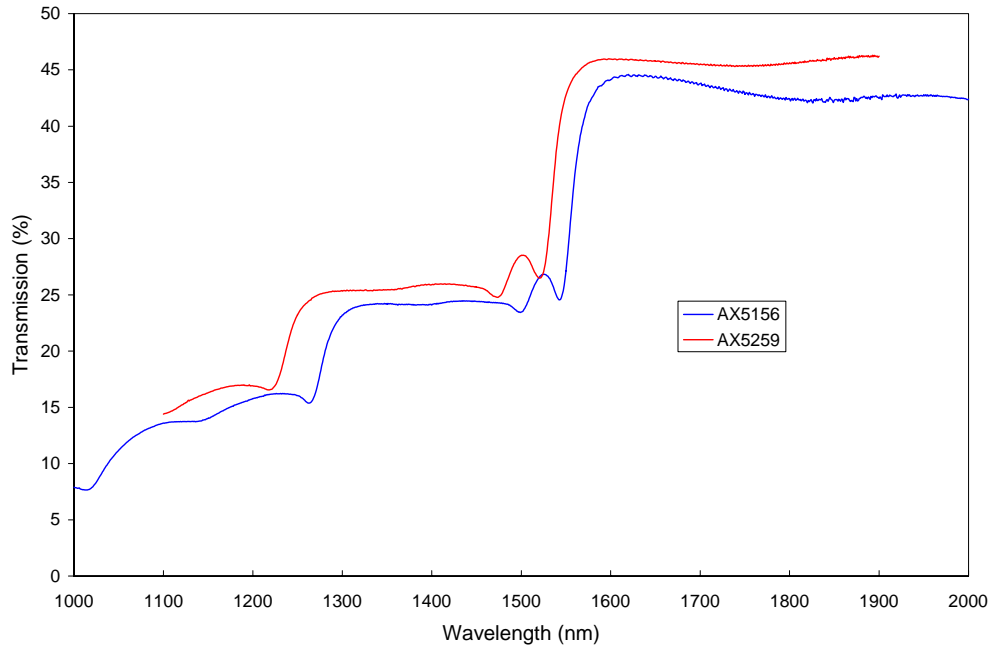
Figure 13. Transmission spectra for saturable absorber samples.

Following calibration of the mirror and absorber the full BRET structure was grown. The total cavity length is ~360 nm from the modeling. Three structures were grown, two with nominally this thickness and one with nominally 370 nm thickness. The samples were backside polished. The backside was anti-reflection coated and the front side had a dielectric mirror deposited. The dielectric DBR consisted of 4 pairs of Si/Al_2O_3 to give a peak reflectivity of ~98%. Transmission measurements should show a sharp resonance peak at about 1570 nm. Reflectivity measurement results for these 3 structures are shown in Figure 14. Sample AX5264 has the resonant peak closest to the intended 1570 nm.
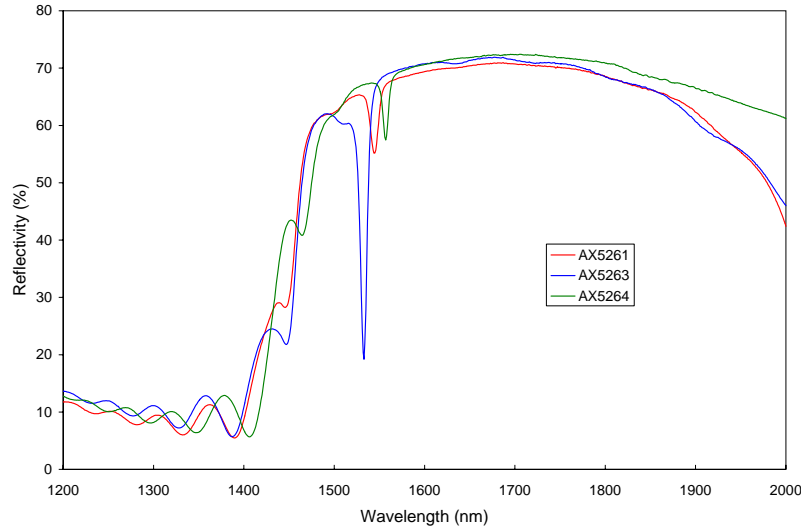

Figure 14. Reflectivity spectra for full BRET structures.

Measurement of the Transfer Characteristics

Nonlinear transmission measurements were carried out. In an attempt to avoid temperature effects, a pulsed setup was used (Figure 15). Transmission through the sample was recorded by detecting the transmission of the ~150 ns optical pulses through the sample. CW light from a tunable laser is amplified with a semiconductor amplifier (SOA) and focused onto the sample (~3-4 μm spot size). Optical pulses are obtained by driving the SOA with electrical pulses. The transmission is detected with a high-speed photo diode and recorded with a digital oscilloscope. A reference signal has been recorded by removing the sample from the setup. Figure 16 shows the recorded traces of the reference signal, and the transmission measured through the sample at two wavelengths. Plotting reference signal versus transmission signal produces the transfer curves as shown in Figure 17. The shape of the transfer characteristics depends strongly on the wavelength. An opening in the trace is visible too. A step like behavior was not observed.

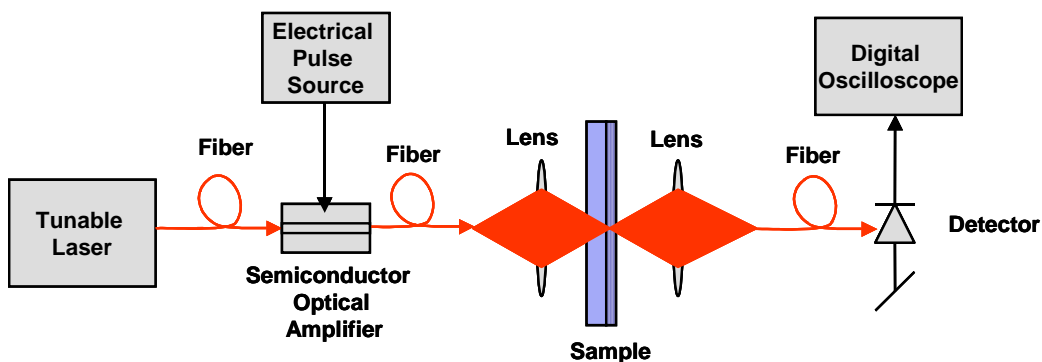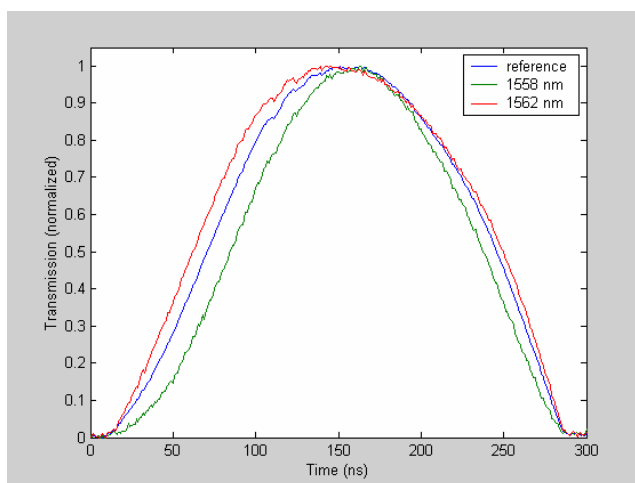**Figure 15.** Setup for measuring the transfer characteristics of the BRET devices.

Figure 16. Recorded signals: Blue - reference measured without sample. Green - with sample, wavelength set to 1558 nm. Red - with sample, wavelength set to 1562 nm.
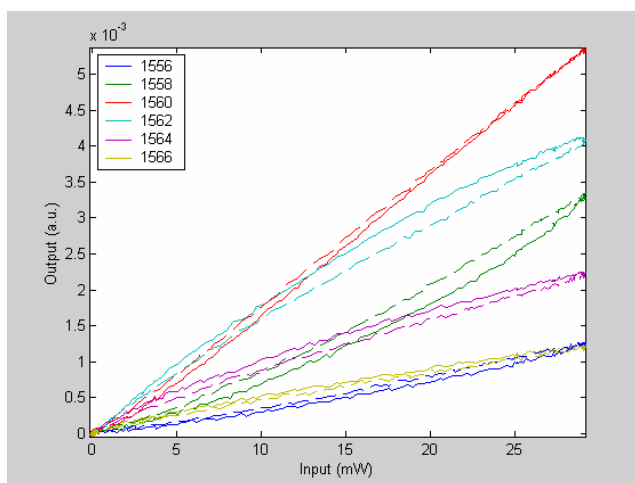

Figure 17. Input power versus output power at different wavelengths (1556-1566 nm). Solid part of the curves is the rising edge; the dashed part is the falling edge.

The cavity reflectivity spectrum at low optical power was modeled and compared with measured reflectivity data. Figure 18 compares the modeled and measured data for one of the samples (AX5263). The optical absorption of the quaternary mirror near its band edge ($\lambda = 1.4$ µm) and the change of index was modeled.
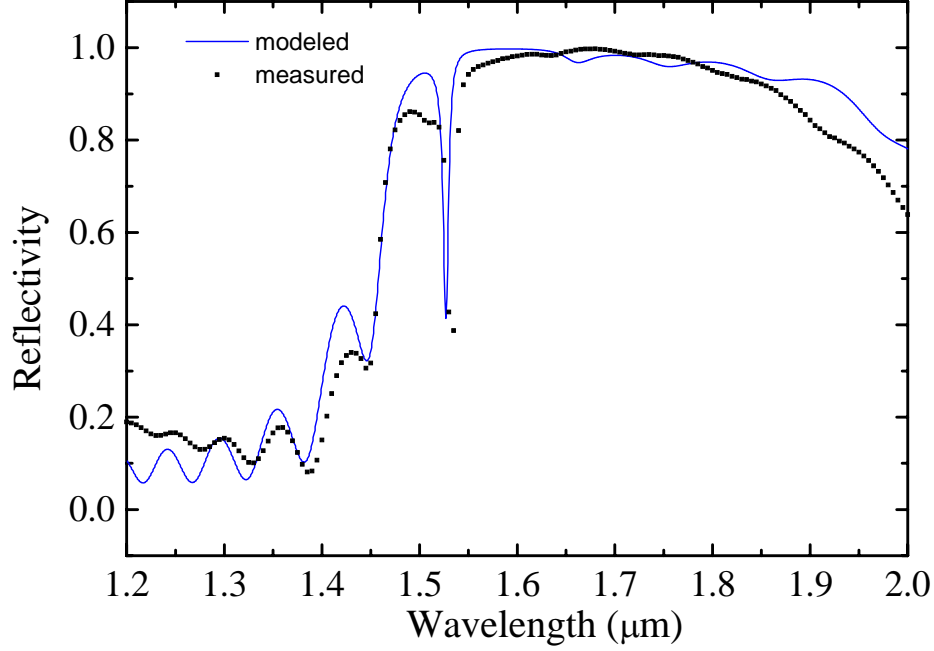
Figure 18. Measured and modeled reflectivity of the cavity from the dielectric mirror side.

The following conclusions were made from the modeling of the low intensity reflectivity:

- The dielectric mirror reflectivity is about 99.8% (Figure 19-a).

- The ripples above 1.5 µm could only be explained by assuming a loss of ~1000 cm^{-1} in the dielectric mirror stack. The loss might be due to roughness and hence scattering.

- The semiconductor Bragg mirror has a reflectivity of about 97% at $\lambda = 1550$ nm (Figure 19-b). The reflectivity drops to 95% for a detuning of ~20 nm.

- Material loss in the cavity cannot be more than ~200 cm^{-1}.

(a)   (b)

Figure 19. Modeled reflectivity spectra of (a) dielectric, and (b) semiconductor Bragg mirrors.

Assuming that the active layer material has the designed bandgap, the linear loss inside the cavity must be much higher than $200\,cm^{-1}$. Therefore, a natural conclusion is that the material bandgap is blue-shifted. We could simulate input-output characteristics with a similar curvature as the measured data by assuming a nearly 40 nm blue shift in the bandgap (Figure 20). Note that this model is "stati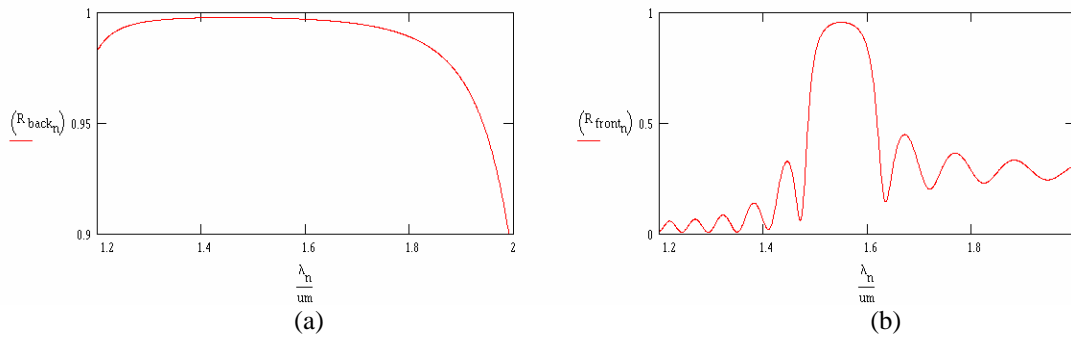c" and cannot simulate the dynamic response of the system. For instance, it cannot simulate the loops in the measured input-output characteristics. These features could not be due to bistability, since they have no clear threshold. Our speculation is that the loops are a result of a delay-type effect in the samples.
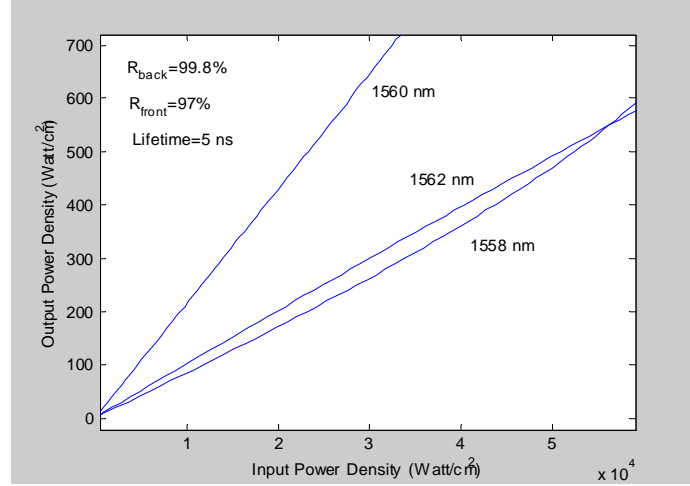
Figure 20. Modeled input-output characteristics of the device at different wavelengths.

More detailed measurements were taken on the first iteration of BRET structures. The test set-up was optimized as shown in Figure 21 to get an improved signal to noise ratio. No bistability was observed on any of the three samples. Typical results for two different samples are given in Figures 22 and 23.
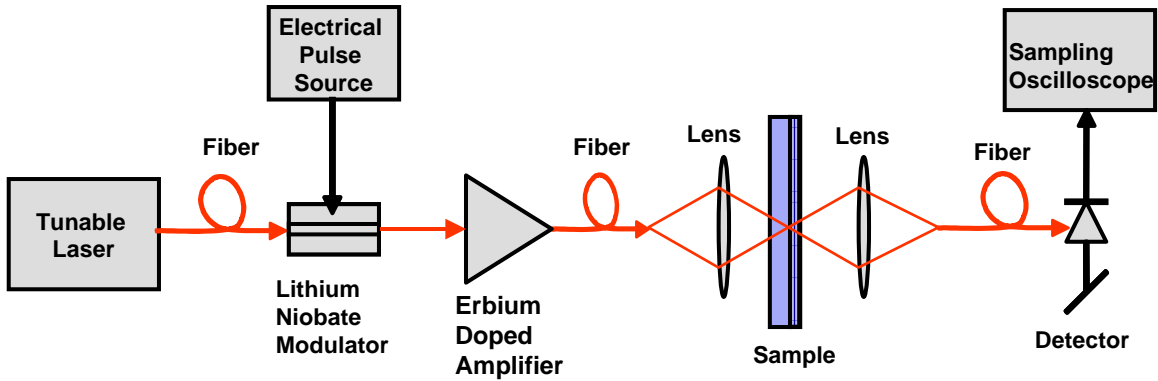
Figure 21. Improved measurement test set-up.
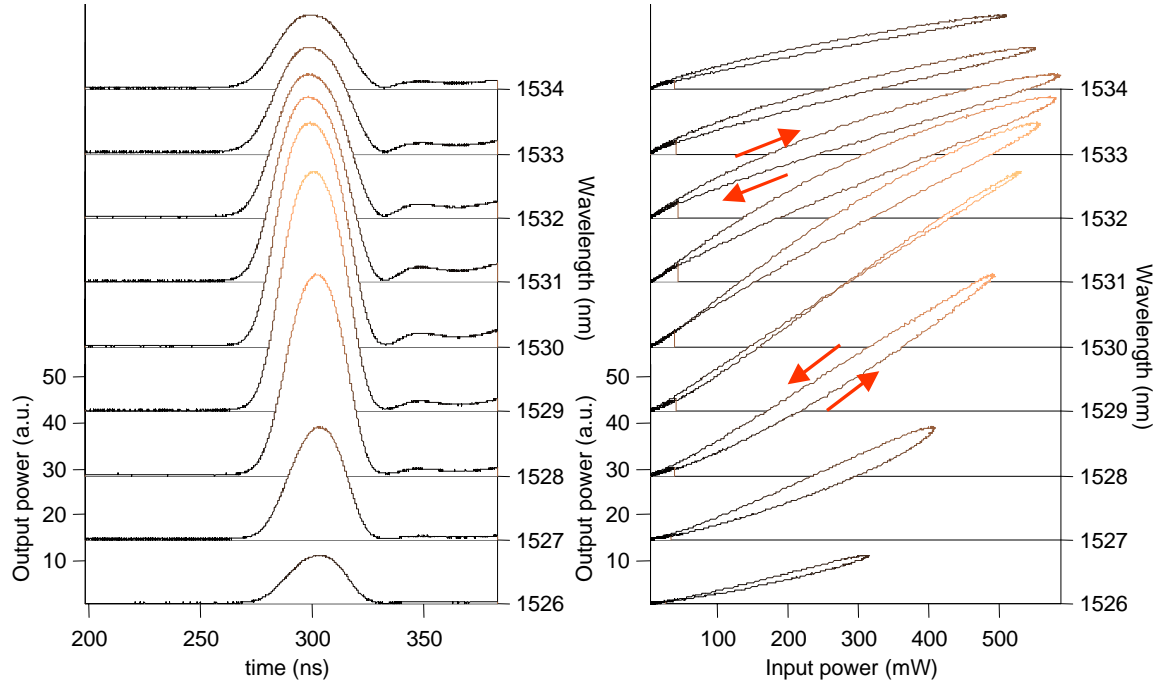
Figure 22. Nonlinear transmission data for sample AX5264, spot-size ~ 5 m.
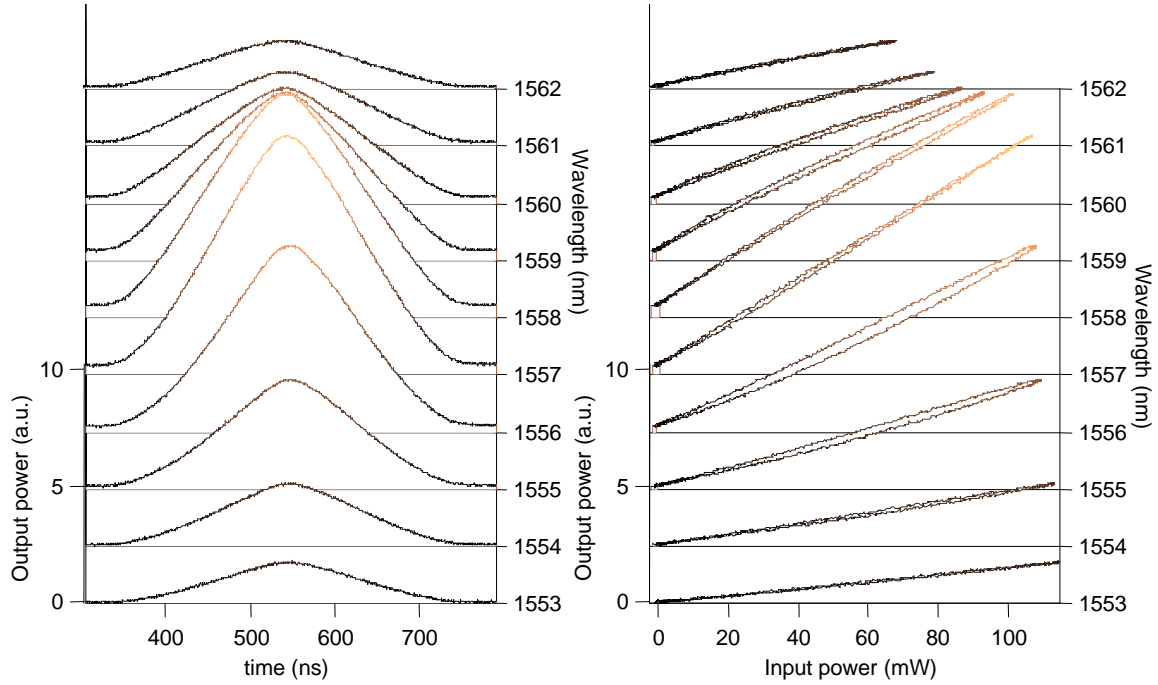
Figure 23. Nonlinear transmission data for sample AX5261, defocused, spot-size ~ 20 m.

Modeling simulated input-output characteristics with a similar curvature as the measured data by assuming a nearly 40 nm blue shift in the bandgap. This appears to be a possible issue with the first iteration, which may have prevented bistability.

<u>Second Growth Iteration</u>

A second growth iteration that addressed several issues with the first iteration was planned and discussed with AFRL. The wavelength of the active region was shifted to longer wavelength. Issues with quality of the dielectric mirror were addressed. Particular issues were as follows:

1. The semiconductor DBR must have an absorption edge that is far enough from the 1550 nm light. Peak PL of the quaternary must be 1400 nm at the longest. A DBR with 22 pairs of 122.85 nm InP and 113.33 nm InGaAsP (1400 nm) should give >97% reflectivity from 1540 nm to 1570 nm.

2. We needed to have one sample with an active layer of Al-free quaternary QW to make sure that the active layer was OK. Absorption in the range of 200-1000 cm^{-1} (at low intensity) is desirable. The peak PL of the MQW must be ~1500 to 1520 nm at the center of the sample.

3. The active layer of InGaAs/InAlAs needed to have a peak PL of 1530 to 1550 nm at the center of the sample.

4. A growth run to test the wavelength shift of the quantum wells grown on the DBR stack was needed. A layer of quaternary InGaAsP with a composition similar to the "average" composition of the mirror and a thickness equal to the total thickness of the mirror was grown before the active region. This should provide a similar growth effect while preventing a "cavity" effect, allowing a good photoluminescence measurement. A shift of approximately 10 nm to shorter wavelength was observed. This was taken into account during actual structure growth.

5. In order to address cleanliness issues of the front surface after polishing, the HR coating was deposited on the wafers before polishing. Then the backside was polished and the AR coating was deposited on the polished surface.

6. The dielectric mirror was changed to <u>three</u> pairs of Al$_2$O$_3$ (255.76 nm) and Si (111.07 nm). The reflectivity should be 99.1% over a very wide wavelength range.

Three structures were grown during the second iteration. The wavelength of the active region was shifted to longer wavelength for all structures. Two structures contained InGaAs/InAlAs active regions similar to the first iteration but with a longer resonance peak of the etalon. One structure was grown using Al-free InGaAs/InP for the active region to eliminate possible issues with the Al containing layers.

One half of each wafer from the iteration was coated at Sarnoff with a dielectric mirror comprised of three pairs of Al$_2$O$_3$ (255.76 nm) and Si (111.07 nm). Reflectivity of 99.3% around 1550 nm wavelength range was measured. These half wafers were cleaved into quarters and one quarter of each was sent to AFRL. Testing on these wafers was done at both Sarnoff and AFRL. A second half of each wafer from the iteration was coated externally at Rugate Technologies, Inc. with an 8 pair dielectric stack that should have 99% reflectivity around 1550 nm.

The second iteration was measured with the same set-up as the first iteration. More pronounced nonlinear behavior was observed but again, no bistability was observed. Measurement results are shown in Figures 24 and 25.
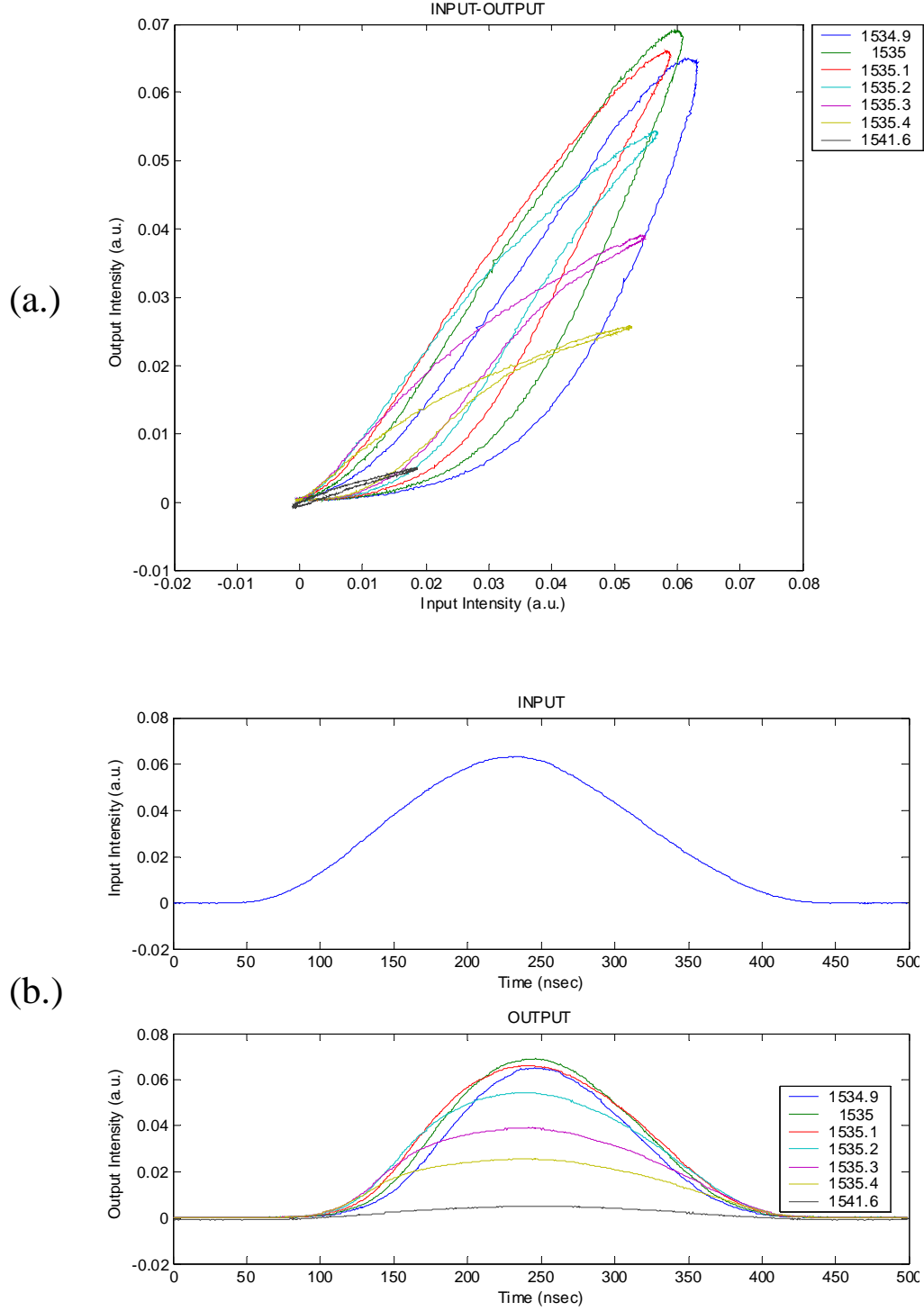
(a.)

(b.)

Figure 24. Input power versus output power (a) and input/output pulses (b) at different wavelengths for sample AX5475.
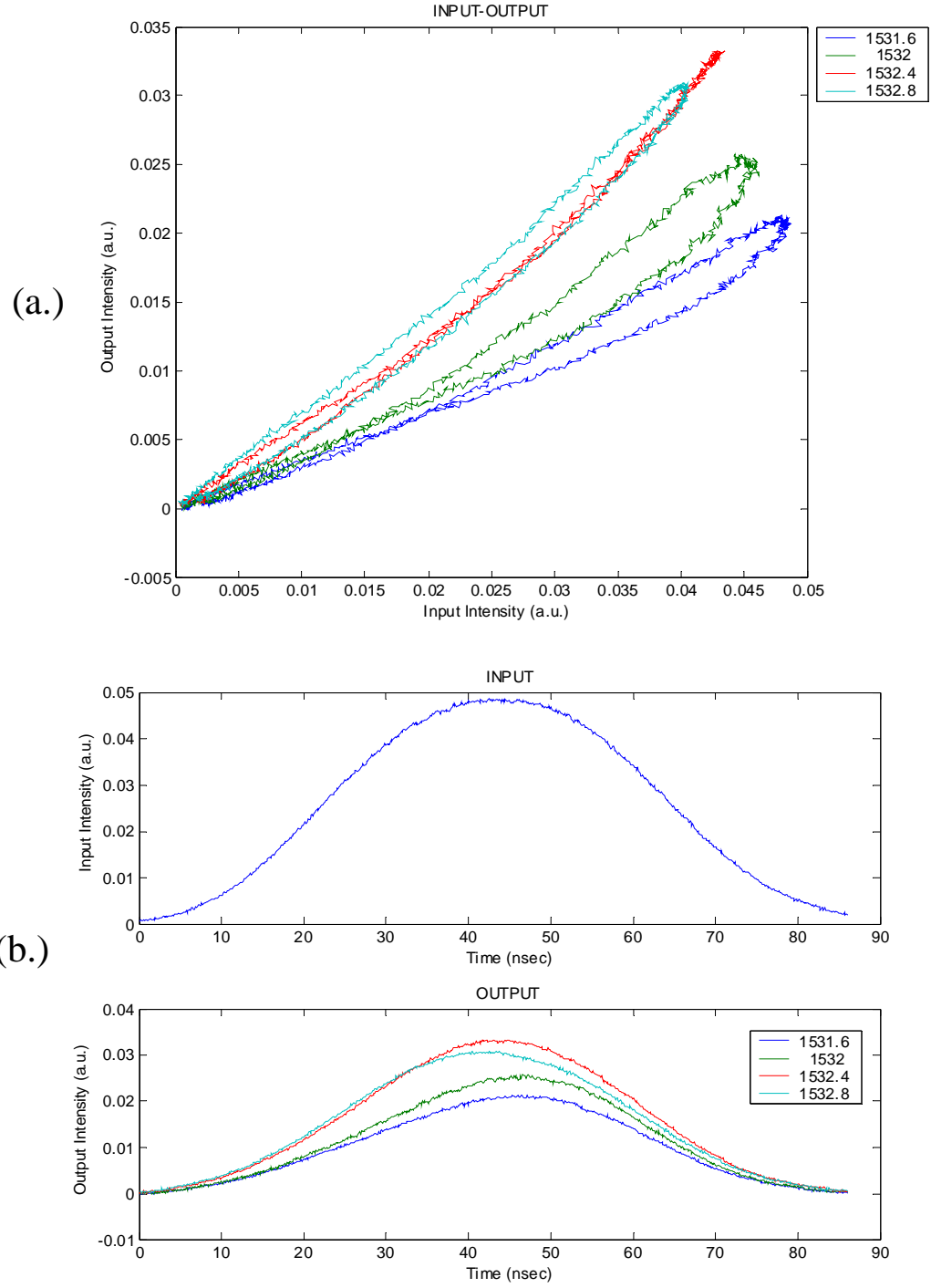
Figure 25. Input power versus output power (a) and input/output pulses (b) at different wavelengths for sample AX5479.

Conclusions and Future Directions

It is our opinion that the main obstacle to bistability in the BRET structure was heating effects as explained in the following list. Our suggestion for a future approach is to use bistable ridge waveguides instead of bistable vertical cavities. We have observed bistability in such devices fabricated for other purposes. The advantages of the ridge waveguide approach are given in the following list:

1. <u>Better heat management</u>: heat generation is an important issue in the bistable devices, since the change of index resulting from the change in temperature can compete with the change of index resulting from the carrier generation. Lower optical threshold power in the ridge waveguide geometry combined with a significantly lower heat resistance make this geometry less susceptible to the heating problem than the vertical cavity. Note that the heating problem can be reduced by decreasing the optical pulse width and duty cycle. However, there is a limit to this method, since the rate of change of temperature versus time is independent of the above and only changes by the material heat capacitance and the beam power. For example, our two-dimensional thermal modeling of a vertical geometry with beam spot size of 5 μm shows that an input power of only 1 mW ($\sim$4kW/cm^2) gives a change of temperature versus time of $\Delta T/\Delta t \sim 7.45 \times 10^7$ K/sec. This means that the temperature will rise about 7°C in only 100 ns. Knowing that $\Delta n/\Delta T$ in the InGaAs quantum wells is about 5×10^{-4} 1/K, one can calculate a change of index of about 3.5×10^{-3} which is comparable to the carrier induced change of index.

2. <u>Higher yield</u>: uniformity of the quantum well thickness and composition limit the thickness of the active layer to less than one micron. In a vertical cavity resonator such thickness leads to a free spectral range of more than 400 nm. This puts a stringent requirement on the cavity thickness accuracy, since only one resonant frequency is close enough to the band edge. Simulation results show that good bistability requires a resonant detuning with accuracy of $\sim$5 nm, which translates into $\sim$5 nm accuracy in thickness or $\sim$0.5%. The typical accuracy of the MOCVD growth is only about a few percent. In the above, we assumed that the bandgap of the active layer is known. In practice however, the bandgap of the active layer changes by about $\pm$5 nm in successive growth runs. Obviously this variation reduces the chance of a successful device even further. The ridge waveguide configuration alleviates these problems by providing a free spectral range in the order of a few nanometers. This means that one can always find a resonance wavelength that is inside the $\sim$5 nm detuning range.

3. <u>Lower optical threshold</u>: change of index versus optical intensity in a quantum well active layer shows a saturation characteristic. Therefore, material sensitivity decreases at higher optical power densities. This means that for a given input optical power, one can obtain a higher total change of phase, if the nonlinear medium is elongated in the optical propagation direction (resulting in a lower optical density). Therefore, bistable ridge waveguides can fundamentally provide a higher sensitivity, and hence lower optical threshold than their vertical counterparts.

4. <u>Better integration</u>: finally, ridge waveguide geometry has obvious advantages compared to the vertical cavity geometry for integration.